research papers

CrossMark

Fast microstructure and phase analyses of nanopowders using combined analysis of transmission electron microscopy scattering patterns

P. Boullay,[a]* L. Lutterotti,[a,b] D. Chateigner[a,c] and L. Sicard[d]

[a]CRISMAT, UMR 6508 CNRS/ENSICAEN, 6 Boulevard du Maréchal Juin, 14050 Caen Cedex, France, [b]Department of Industrial Engineering, University of Trento, via Sommarive 9, 38123 Trento, Italy, [c]IUT-Caen, Université de Caen Basse-Normandie, France, and [d]ITODYS (UMR 7086), Université Paris-Diderot, Bâtiment Lavoisier, 15 rue Jean-Antoine de Baïf, 75205 Paris Cedex 13, France. Correspondence e-mail: philippe.boullay@ensicaen.fr

The full quantitative characterization of nanopowders using transmission electron microscopy scattering patterns is shown. This study demonstrates the feasibility of the application of so-called combined analysis, a global approach for phase identification, structure refinement, characterization of anisotropic crystallite sizes and shapes, texture analysis and texture variations with the probed scale, using electron diffraction patterns of TiO_2 and Mn_3O_4 nanocrystal aggregates and platinum films. Electron diffraction pattern misalignments, positioning, and slight changes from pattern to pattern are directly integrated and refined within this approach. The use of a newly developed full-pattern search–match methodology for phase identification of nanopowders and the incorporation of the two-wave dynamical correction for diffraction patterns are also reported and proved to be efficient.

1. Introduction

The tremendous development of materials science at the nanoscale and the use of nanocrystalline powders (nanopowders) challenges the usual characterization techniques on their ability to properly describe small objects, either individually or as large assemblies. Constituting phases and their various micro- and nanostructural characteristics all are targets for quantitative characterization: structure determination and/or refinement, phase identification and contents (crystalline or amorphous, mixtures), microstructure (isotropic/anisotropic crystallite sizes, shapes and microstrains, defects etc.), preferred orientations (crystallographic texture). Such analyses are routinely done using X-ray and neutron powder diffraction (XPD and NPD, respectively). In the case of nanoparticles, strong line broadenings and overlaps occur and raise difficulties in 'classical' phase identification, structure and microstructure determination, which become less quantitative or even unreliable. Furthermore, with regard to non-homogeneous nanocrystalline materials, local quantitative information on the microstructure may not be easily accessible using very global approaches like XPD and NPD, not to mention the often very small quantities of materials, preventing use of any X-ray and neutron methods. In such cases, transmission electron microscopy (TEM) is one of the few techniques able to provide quantitative results using imaging, spectroscopic or diffraction methods. Aiming at the

structure, size and phase analysis of nanoparticles, a TEM approach would ideally combine both imaging and diffraction at the nanometre scale.

The imaging capabilities obtainable in a modern transmission electron microscope can indeed provide direct observation of the morphology and structure of nanoparticles. Likewise, electron nanobeam diffraction (NBD) can be used to acquire diffraction patterns from a single nanoparticle in a scanning transmission electron microscope (Cowley, 2004). Combining these two techniques is possible (Alloyeau et al., 2008; Ganesh et al., 2010) but such analyses on individual particles are not ideal if one wants a representative statistical analysis. They are also not applicable when nanoparticles are agglomerated. Another approach would be based on the quantitative analysis of electron diffraction intensities similarly to what is done in XPD and NPD. Indeed, selected-area electron diffraction (SAED) patterns of an assembly of nanoparticles usually exhibit ring patterns analogous to those from XPD, hereafter called electron powder diffraction (EPD) patterns. Phase identification and structure refinement of such powder diffraction patterns can be attained by standard X-ray diffraction (XRD) analysis based on search–match routines followed by Rietveld analysis (Rietveld, 1967) or PDF (pair distribution function) (Proffen & Billinge, 1999) methods. The role of EPD in solving structures is limited but the feasibility of structure refinement using the Rietveld method (Weirich et al., 2000, 2002, 2006; Tonejc et al., 2002; Kim et al., 2009; Song

et al., 2012) as well as the possibility of obtaining reliable atomic PDFs (Abeykoon et al., 2012) have already been demonstrated.

The present work focuses on the quantitative analysis of EPD of nanoparticle assemblies and, generally speaking, of nanostructured materials. Besides the structure-refinement issue, we will show that the average size and shape of the crystallites as well as quantitative texture analysis (QTA) can be obtained from EPD using Rietveld analysis within the combined analysis methodology (Chateigner, 2010) as implemented in the MAUD (Material Analysis Using Diffraction) software (Lutterotti et al., 1997; Lutterotti, 2010). The results are discussed and compared to X-ray diffraction patterns, measured on TiO_2 and Mn_3O_4 nanopowders. We use these case studies to illustrate how dynamical effects can reasonably be taken into account in Rietveld modelling in such circumstances of small crystals.

2. Experimental

XPD diagrams were either measured in reflection or transmission modes using an INEL with a CPS120 detector at fixed incident angle (Morales et al., 2002), or D8 Bruker and LYNXEYE detector and capillary diffractometer setups, respectively. In both cases monochromated Cu K radiation was used. X-ray instrument line-broadening contributions, $g_{XR}(x)$, were determined using the LaB_6 standard sample from NIST (660b standard reference material).

EPD patterns were obtained from several electron microscopes including a Jeol 2010 (200 kV), a TOPCON 002B (200 kV) and an FEI Tecnai G2 (300 kV). They were equipped with Gatan CCD cameras: an Orius SC200D (2048 × 2048 pixels, 7.4 µm each) for the first two and an Ultrascan 1000 (2048 × 2048 pixels, 14 µm each) for the Tecnai.

Mn_3O_4 hausmannite and TiO_2 rutile nanopowders were prepared according to the process described in Sicard et al. (2010) and Reddy et al. (2006), respectively. A small quantity of the powder was dispersed in alcohol and a drop of the suspension was deposited on an amorphous carbon film supported by a copper grid.

The Rietveld analysis of EPD patterns was carried out in MAUD using electron atomic scattering factors from Peng et al. (1996). Intensity integration along the Debye rings was performed using ImageJ plugins implemented directly in MAUD (see supporting information[1]) which allow the import of two-dimensional diffraction data coming from CCD or imaging-plate detectors (Ischia et al., 2005; Lutterotti et al., 2007; Lutterotti, Vasin & Wenk, 2014) without external processing, for example using ELD (Calidris, Sollentuna, Sweden) (Weirich et al., 2000, 2002, 2006; Tonejc et al., 2002;

[1] Details of EPD intensity extraction in MAUD (Lutterotti, 2010; Lutterotti, Vasin & Wenk, 2014; Williams & Carter, 1996), phase identification using the full-pattern search–match procedure (Lutterotti, Pilliere et al., 2014; Gražulis et al., 2009; Downs & Hall-Wallace, 2003; Lutterotti et al., 2013; Database of Zeolite Structures, 2014) and the Blackman correction implemented in MAUD (Blackman, 1939; Sinkler et al., 2007; Spence & Zuo, 1992; Palatinus et al., 2013; Li, 2010; Peng et al., 1996) are available from the IUCr electronic archives (Reference: IB5025).

Kim et al., 2009; Song et al., 2012) or FIT2D (Hammersley, 1998; Gemmi et al., 2011). In MAUD the data are imported preserving the original image coordinate position for each data point. Using more patterns around the beam centre enables the program to refine the centre displacement and image tilting errors directly in the Rietveld analysis (Lutterotti, Vasin & Wenk, 2014). Two ways of data-set plotting can be used. The first one is a two-dimensional plot where all the 2θ patterns are displayed on top of each other with the η–azimuthal variation along the ordinate and colour-levelled scattered intensities. The second kind of plot is a sum of all the caked one-dimensional plots, i.e. a full integration along the Debye rings.

3. Phase search/match and phase analysis

From the measured profile $h(x)$, peak location and intensity characteristics of a given structure can be used as a fingerprint to perform automated phase identification, provided the phase (or an isostructural one) is known and listed in a database. Automatic phase search and match procedures based on X-ray powder diffraction data are widely used in the materials science community. Similar identification of crystalline phases using the XRD-like profile extracted from EPD has already been described and used in a few software programs. EDSEARCH (Carr et al., 1986) and RINGS (Denley & Hart, 2002) utilize a d-spacing search/match procedure from NIST databases while ProcessDiffraction (Labar, 2009) and PCED2.0 (Li, 2010) proceed through a comparison of the experimental peak positions with possible candidate structures available in the JCPDS or ICSD databases but without a search/match procedure.

With regard to nanocrystalline materials, phase identification based on the analysis of powder diffraction patterns meets with a difficulty due to severe line broadening creating strong overlaps between peaks. In such cases peak positions are hard to detect precisely using a simple peak maximum search. To overcome this, the authors propose an automated search/match procedure based on a full-pattern fitting (i.e. Rietveld fit) accounting for peak broadening and applicable to XPD, NPD and EPD patterns (Lutterotti, Pilliere et al., 2014). This full-pattern search–match procedure can be efficiently used for phase identification from intensities integrated along the EPD rings (see supporting information).

4. Peak broadening: average size and shape

Line broadening in the measured profile $h(x)$ can be decomposed as the convolution of the instrumental broadening $g(x)$ and the sample contribution $f(x)$ plus a background function $b(x)$: $h(x) = f(x) \otimes g(x) + b(x)$. For $b(x)$ we use a polynomial function plus an additional Gaussian peak at 0° 2θ in order to model the strong increase of the background at low angle due to the primary transmitted beam. No pre-treatment such as removing the contribution of the C-supporting film is done (Kim et al., 2009). When using the Rietveld method for structure refinement only, the terms $f(x)$ and $g(x)$ can be fitted

as one single contribution for line broadening where sample contributions such as preferred orientation can still be accounted for. When these microstructural effects are quantitatively estimated, broadening contributions from the sample and instrument must be separated during the Rietveld refinement. A large and comprehensive literature about this procedure, widely used in X-ray powder diffraction, can be found (Chateigner, 2010).

Conventionally, in X-ray powder diffraction experiments, one uses a reference sample with crystallite sizes that are large enough and isotropic, and crystallite shapes with negligible microstrains. Such a sample consequently does not contribute to line broadening and any broadening in the corresponding diffraction pattern is solely due to the instrument. In electron diffraction, the larger the crystallites, the more discontinuous and grainy will be the ring pattern, making powder standards suitable for X-ray instrumental calibration (LaB_6 for instance) not appropriate. Fortunately, in the case of nanoparticles, the $g(x)$ function can be determined using nanopowders previously calibrated by X-ray measurements. For the present study our reference sample was an aggregate of nanosized Mn_3O_4 crystallites prepared by a polyol process and known to be single phase with uniform crystallite sizes (Sicard *et al.*, 2010). The first step of the calibration procedure is to determine $f_{XR}(x)$, *i.e.* here the average size and shape of the crystallites using an X-ray powder diffractometer with a known instrumental function $g_{XR}(x)$:

$$h_{XR}(x) = f_{XR}(x) \otimes g_{XR}(x) + b_{XR}(x).$$

In this step, since $g_{XR}(x)$ is measured using the large crystals of LaB_6, it satisfies the requirement for a good resolution on the determination of nanosized crystallites, in X-ray as well as in later TEM measurements. Obtaining $f_{XR}(x)$ has been done on a Bruker D8 linear-focus diffractometer and, as a test, we have used two geometries for data collection: reflection mode (collection time: 3.5 h) with all the powder at our disposal, *i.e.*

Table 1
Reliability factors and cell-parameter refinements resulting from the size and shape analyses of Mn_3O_4 and TiO_2 nanopowders.

PM stands for pattern matching (Le Bail decomposition). Kinematic indicates that kinematical approximation is used for structure-factor calculations and Blackman with a two-wave dynamic correction.

	R_w (%)	R_{Bragg} (%)	a (Å)	c (Å)
Mn_3O_4 (No. 141: $I4_1/amd$), Popa coefficients up to R_3 (see Fig. 2)				
XRD	5.83	4.63	5.764 (2)	9.448 (4)
EPD PM	1.70	1.27	5.7649 (2)	9.4267 (4)
EPD kinematic	2.60	2.03	5.7656 (3)	9.4113 (6)
EPD Blackman	2.07	1.58	5.7639 (2)	9.3996 (5)
TiO_2 (No. 136: $P4_2/mnm$), Popa coefficients R_0 and R_1 (see Fig. 3)				
XRD	2.49	1.96	4.584 (1)	2.949 (1)
EPD PM	2.30	1.65	4.5875 (2)	2.9475 (2)
EPD kinematic	4.12	3.18	4.5853 (3)	2.9448 (3)
EPD Blackman	3.60	2.65	4.5897 (3)	2.9450 (2)
TiO_2 (No. 136: $P4_2/mnm$), Popa coefficients up to R_4 (see Fig. 4)				
XRD	2.40	1.89	4.585 (1)	2.950 (1)
EPD PM	2.32	1.69	4.5883 (2)	2.9479 (2)
EPD kinematic	3.80	2.89	4.5868 (3)	2.9467 (2)
EPD Blackman	3.33	2.45	4.5920 (3)	2.9458 (2)

~100 mg of Mn_3O_4 hausmannite, and transmission mode (collection time: 6 h) with a smaller powder quantity in a capillary. For this latter mode the signal-to-noise ratio is clearly too bad to allow any microstructural characterization. In a previous study (Sicard *et al.*, 2010), the acquisition time in reflection mode used to characterize similar Mn_3O_4 nanopowders was more than 2 d. In striking contrast, the acquisition time in the transmission electron microscope of a suitable EPD is about a few seconds and a much smaller amount of powder is needed. The result of the analysis of the Mn_3O_4 nanopowder using the Bruker D8 data acquired in reflection mode is illustrated in Fig. 1(*d*). The average size of around 6 nm and roughly cubic shape, fitted using Popa rules (Popa, 1998), are in perfect agreement with previous results (Sicard *et al.*, 2010) and with the apparent size observed in imaging mode with the transmission electron microscope (Fig. 1*e*). Once the sample contribution $f_{XR}(x)$ was obtained, we used it as an input in the analysis of the EPD to extract the instrumental peak shape function $g_{TEM}(x)$ (Fig. 1):

$$h_{TEM}(x) = f_{XR}(x) \otimes g_{TEM}(x) + b_{TEM}(x).$$

The instrumental peak shape function is obtained from EPD using pattern matching (Fig. 1) since this mode allows the best fit of the EPD and, presumably, allows one to get the most reliable estimation of the instrumental function. For the TOPCON 002B used here, the $g_{TEM}(x)$ is modelled using a Caglioti function with $U = 3.32 \times 10^{-4}$, $V = -2.5 \times 10^{-2}$ and $W = 3.2$. Then, keeping the instrumental function fixed, we have
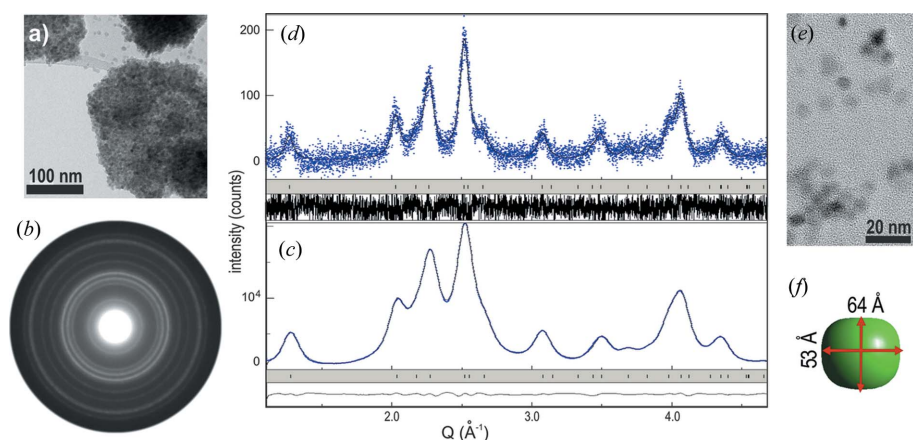

Figure 1
(*a*) Mn_3O_4 nanoparticle aggregates. Associated EPD in (*b*) and one-dimensional plot in (*c*) representing the full integration along the Debye rings. The profile $h_{TEM}(x)$ is fitted ($R_w = 2.06\%$ and $R_{Bragg} = 1.55\%$) by refining the instrumental broadening $g_{TEM}(x)$ using the known sample contribution $f_{XR}(x)$. (*d*) XRD patterns used to extract $f_{XR}(x)$ ($R_w = 5.83\%$ and $R_{Bragg} = 4.63\%$). (*e*) TEM bright-field image of isolated particles. (*f*) Average size and shape of the Mn_3O_4 nanoparticles obtained using two Popa coefficients (R_0 and R_1).

checked the consistency of the samples' characteristic $f_{TEM}(x)$ obtained from EPD using

$$h_{TEM}(x) = f_{TEM}(x) \otimes g_{TEM}(x) + b_{TEM}(x).$$

We tested the feasibility of such a 'two-step calibration' within the combined analysis frame to analyse EPD, using three approaches for the whole-pattern-fitting procedure: simple pattern matching (using the Le Bail method), kinematical approximation for structure-factor calculations, and Blackman two-wave dynamic correction (Blackman, 1939) implemented in *MAUD* (see supporting information). Average crystallite
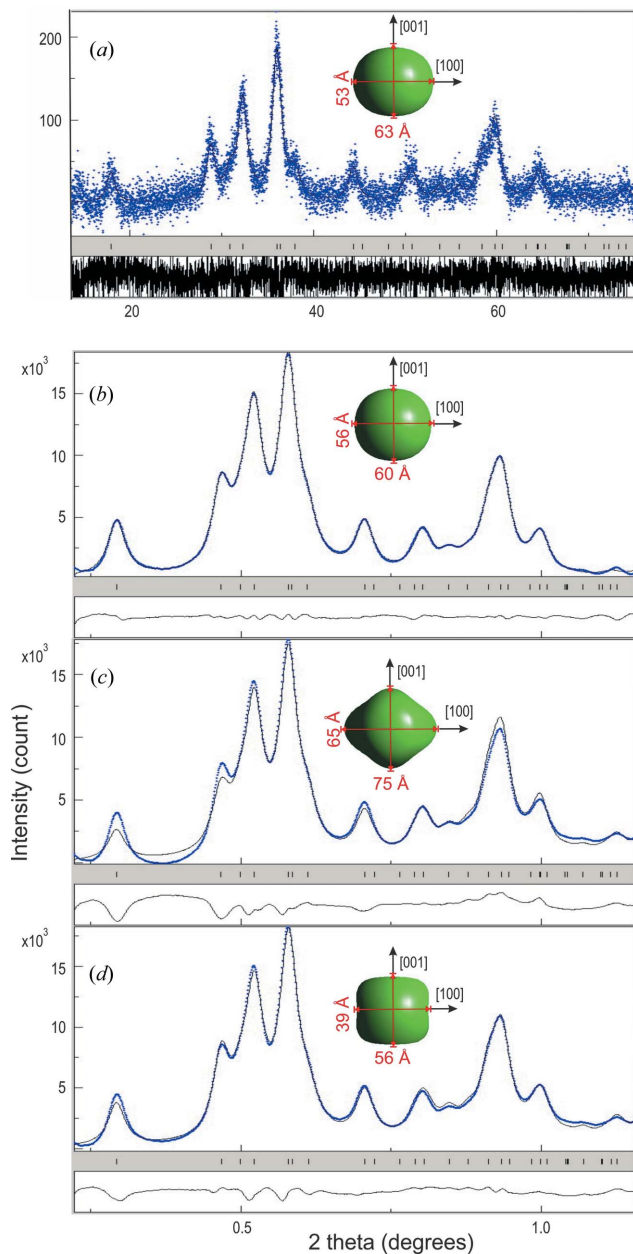
Figure 2
Results of the combined analysis of Mn_3O_4 nanopowders for (*a*) XRD and EPD patterns treated (*b*) using a pattern-matching mode (Le Bail), (*c*) using kinematical approximation and (*d*) using kinematical approximation with Blackman two-wave dynamic correction. The average size and shape estimated from the refinement of Popa coefficients (up to R_3) are given.

sizes and shapes were refined using these three approaches (Fig. 2 and Table 1). The solution found using the Blackman correction gets closer to the one obtained in pattern-matching mode (Table 1). The kinematical approximation leads to a slightly worse pattern fitting with an average size and shape that deviate from those estimated using X-rays (Fig. 2). This is a strong indication that we need to match the intensities sufficiently well to get reliable microstructure results and that a strong correlation exists between intensities and line broadening in the case of nanocrystalline materials with large peak overlap. In Table 1, the lattice parameters refined for the Mn_3O_4 nanopowders are reported. Clearly, the standard deviations obtained from EPD are largely under-estimated and, actually, the accuracy of lattice parameters refined from EPD is less than that obtained from XPD. Nevertheless, the whole-pattern-fitting approach used here to analyse EPD permits us to obtain cell parameters from nanopowders within an accuracy of a few ‰ (see also in Table 1 results obtained for TiO_2).

The second test was performed using TiO_2 rutile nanoparticles (Reddy *et al.*, 2006) presenting an anisotropic shape and available in a larger amount suitable for a fine microstructural analysis using our four-circle high-resolution X-ray
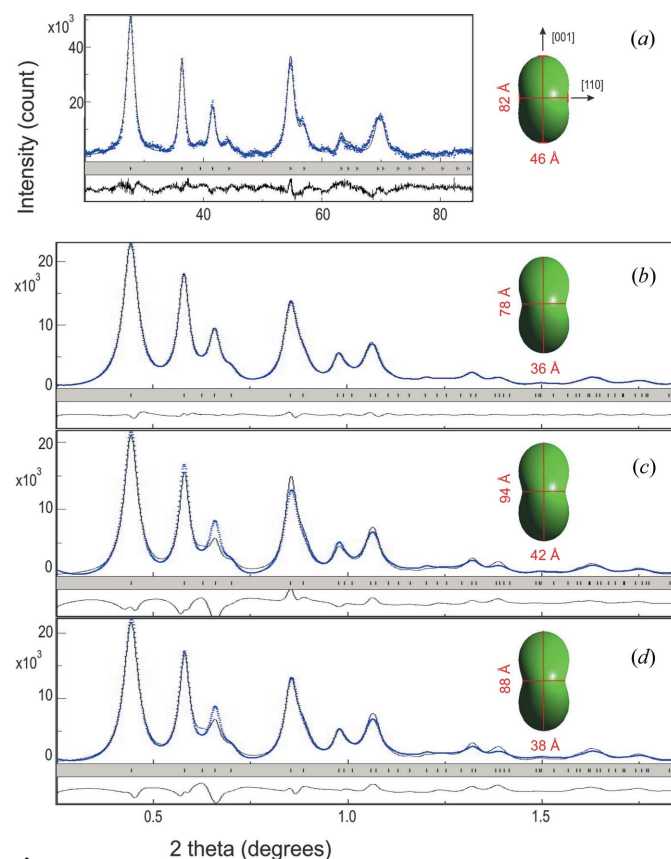

Figure 3
Results of the combined analysis of TiO_2 nanopowders for (*a*) XRD and EPD patterns treated (*b*) using a pattern-matching mode (Le Bail), (*c*) using kinematical approximation and (*d*) using kinematical approximation with Blackman two-wave dynamic correction. The average size and shape estimated from the refinement of Popa coefficients (R_0 and R_1) are given.
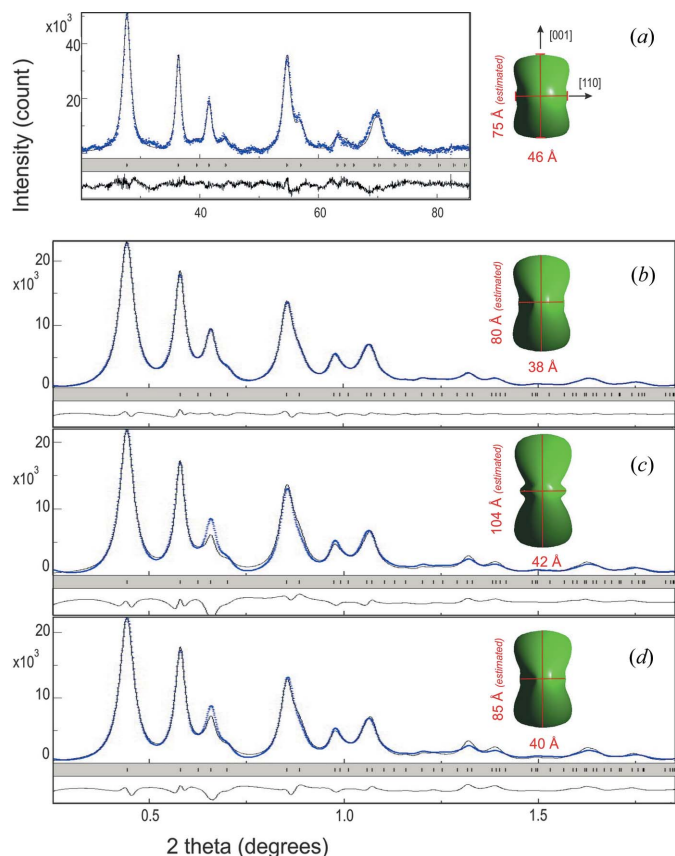
Figure 4
Results of the combined analysis of TiO$_2$ nanopowders for (*a*) XRD and EPD patterns treated (*b*) using a pattern-matching mode (Le Bail), (*c*) using kinematical approximation and (*d*) using kinematical approximation with Blackman two-wave dynamic correction. The average size and shape estimated from the refinement of Popa coefficients (up to R_4) are given.

average shape of the crystallites. In the Popa model used for the 4/*mmm* Laue group, the crystallite shape $\langle R_{\mathbf{h}} \rangle$ is decomposed into R_i coefficients for the size variations with the $\mathbf{h} = [hkl]$ directions using harmonic series:

$$\langle R_{\mathbf{h}} \rangle = R_0 + R_1 P_2^0(x) + R_2 P_4^0(x) + R_3 P_4^3(x) \cos 3\varphi$$
$$+ R_4 P_4^3(x) \sin 3\varphi + R_4 P_6^0(x).$$

Here the first coefficient R_0 gives a crystallite size value representing the average radius of spherical (isotropic) crystallites. Allowing the shape decomposition up to two coefficients R_0 and R_1 (Fig. 3 and Table 1) already achieves an acceptable fit of the patterns both using X-ray and TEM patterns, and a good estimation of the size and shape of the TiO$_2$ rutile crystallites as smooth cylinders with an aspect ratio of about 2. Adding more harmonic coefficients (Fig. 4 and Table 1) did not change drastically either the envelope or the mean size defining the crystallites, but showed a tendency to reveal a more diabolo-like shape. For the kinematic case in which the average size and shape deviate from those estimated by XRD, non-realistic crystallite shape deviations are observed which tend to compensate relatively worse intensities. Using either pattern matching or kinematical approximation with Blackman correction, refinements lead to crystallite morphologies consistent with the one 'certified' by XRD. We furthermore collected EPD patterns for TiO$_2$ (rutile) on different electron microscopes (Jeol 2010, TOPCON 002B and FEI Tecnai G2) and this two-step procedure reproduced identical results, *i.e.* within a given resolution and for small enough crystallites this approach can provide a good estimate of TEM instrumental functions.

A distinctive feature of EPD compared to XRD analysis of nanoparticles is that the amount and volume of particles necessary to obtain a diffraction pattern are extremely small, and counting times to achieve good statistics are very low. But another interesting aspect lies in the possibility of reducing the probed volume using smaller selection-area apertures, in order to approach more local measurements and test local microstructural variations. In doing so, the EPD pattern tends to exhibit more graininess with eventually large intensity variations along the Debye rings. This is particularly noticeable when dealing with anisotropic nanocrystal shapes, like in TiO$_2$ nanopowders, that agglomerate in bundles of crystallites aligned along a preferred crystallographic orientation (Fig. 5*d*). Since the *MAUD* software incorporates quantitative texture determination, it enables crystallite size and shape characterizations accounting for such preferred orientations. In the present case, we simultaneously refined textural and microstructural features as usually done in combined analysis. We will further illustrate the application of

diffractometer. We have analysed independently the profiles obtained by XPD (Figs. 3*a* and 4*a*) and EPD (Figs. 3*b*–3*d* and 4*b*–4*d*) by a symmetry-restrained anisotropic model for the
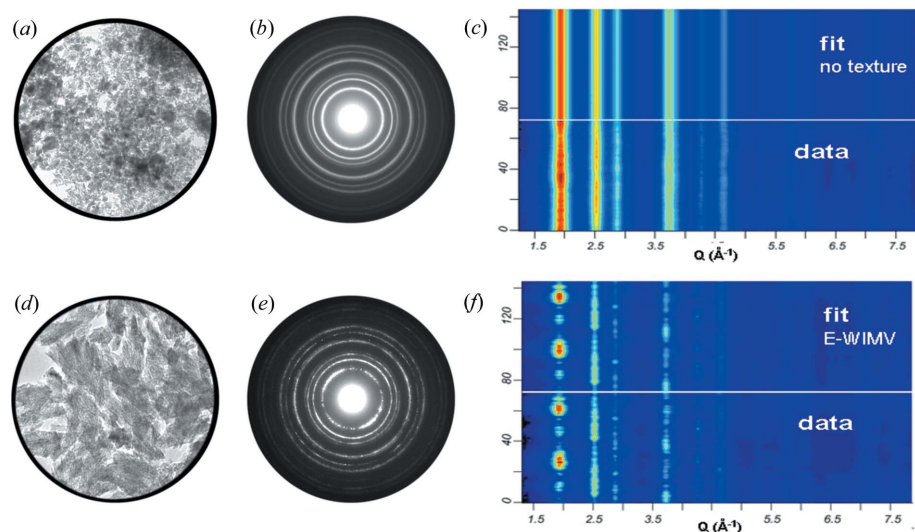

Figure 5
(*a*) 3 μm diameter selected area, (*b*) corresponding EPD and (*c*) two-dimensional plot. (*d*) 0.5 μm diameter selected area, (*e*) EPD and (*f*) two-dimensional plot.

macroscopic texture characterization using combined analysis of EPD patterns in the next section.

Regarding size and shape estimations from peak broadenings using EPD, one should point out that this approach is limited to crystallite sizes much smaller than the ones accessible using laboratory X-rays. These latter, using a middle-resolution diffractometer, are usually limited to sizes not larger than 500 to 1000 nm (X-ray instrument calibrations are often practised using an LaB_6 standard of isotropic crystallite sizes at 2000 nm). For EPD experiments, the spatial resolution is much less, and with the two-step procedure used here, we do not intend to resolve sizes larger than 30 nm at maximum. On the three TEM instruments used in this work we did not find noticeable differences in the instrumental contributions which remain poorer compared to those of X-rays.

5. Textured samples

The analysis of textured electron diffraction patterns has been widely studied since the pioneering work of Vainshtein *et al.* (Vainshtein, 1964). Orientation imaging microscopy (OIM) obtained by electron back-scattered diffraction (EBSD) in a scanning electron microscope is widely used but shows

limitations when the average grain size approaches nanoscale. The TEM orientation and phase-mapping technique recently developed (Rauch & Véron, 2005) allows one to get a better spatial resolution up to nanometre sizes in field-emission TEM. Alternatively, for homogeneous nanopowders with true relevancy of the mean crystallite behaviour, direct use of the diffraction patterns to reach quantitative texture analysis is possible, *i.e.* using the refinement of the orientation distribution function (ODF). In the following we illustrate full-pattern QTA of a Pt thin film deposited on an Si single-crystal substrate.

The TEM pattern collection has to be operated at as many tilt and azimuth angles as possible (Gemmi *et al.*, 2011; Weiland & Panchanadeeswaran, 1993) in order to ensure enough 'coverage' of the ODF, *i.e.* getting enough measurements to achieve a unique solution during the ODF refinement. Indeed, with only one pattern measured at one sample orientation with respect to the electron beam, only a limited number of orientations of the crystallites are probed (Fig. 6a) and most of the time, depending on the crystal and sample symmetries, the ODF is not defined unequivocally. We increased the number of orientation data by varying the tilt angle (from $+25°$ to $-25°$, step $5°$). Using such a data set the
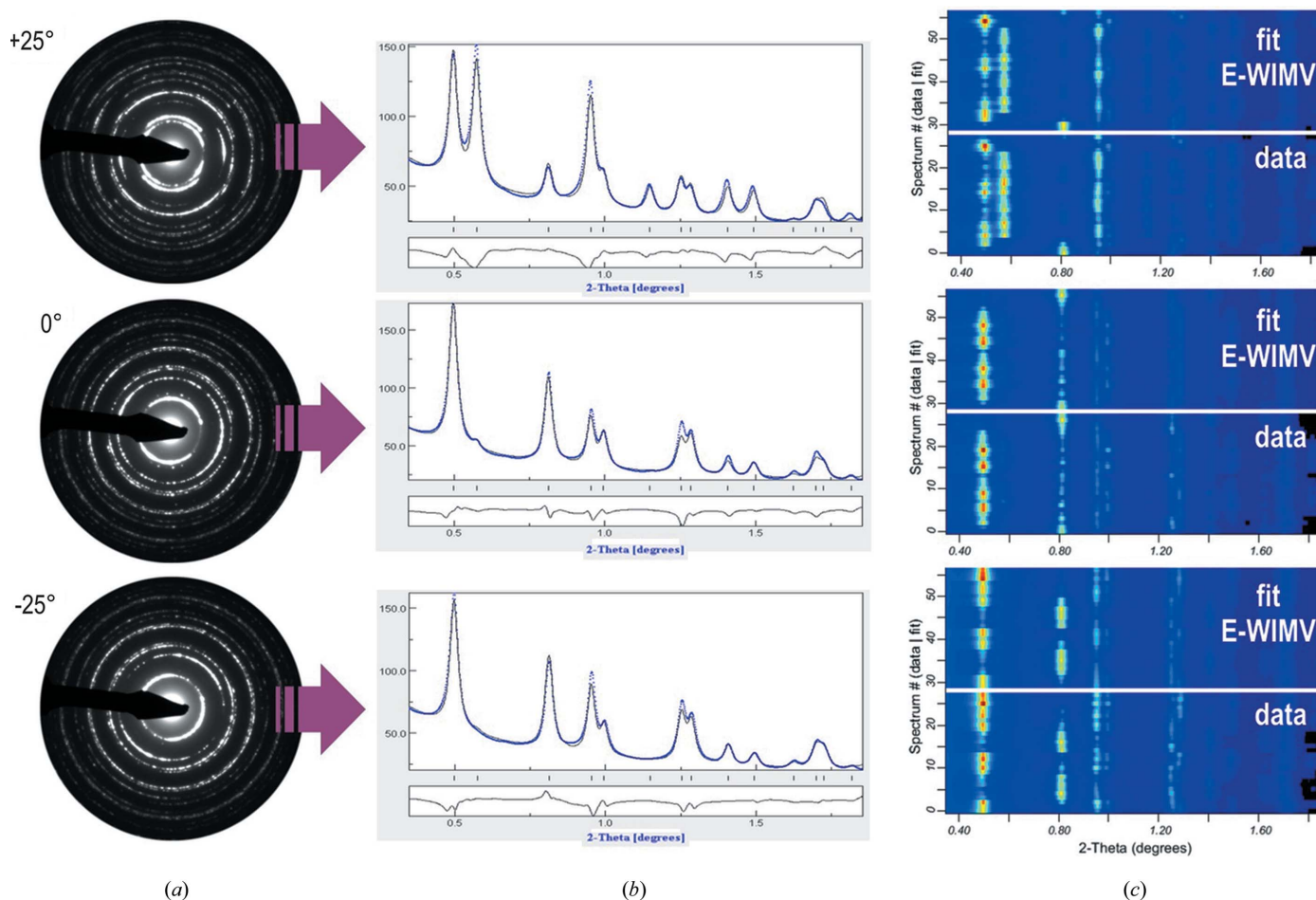

Figure 6
(a) Diffraction patterns for two extreme and $0°$ sample tilts. (b) Corresponding one-dimensional patterns using $\Delta\eta = 10°$ and for $\eta = 180°$. (c) Two-dimensional plots for the 35 one-dimensional patterns of each two-dimensional pattern in (a). Experimental data (bottom) and fits (top) are represented, Pawley pattern matching. Square-root intensity scales.
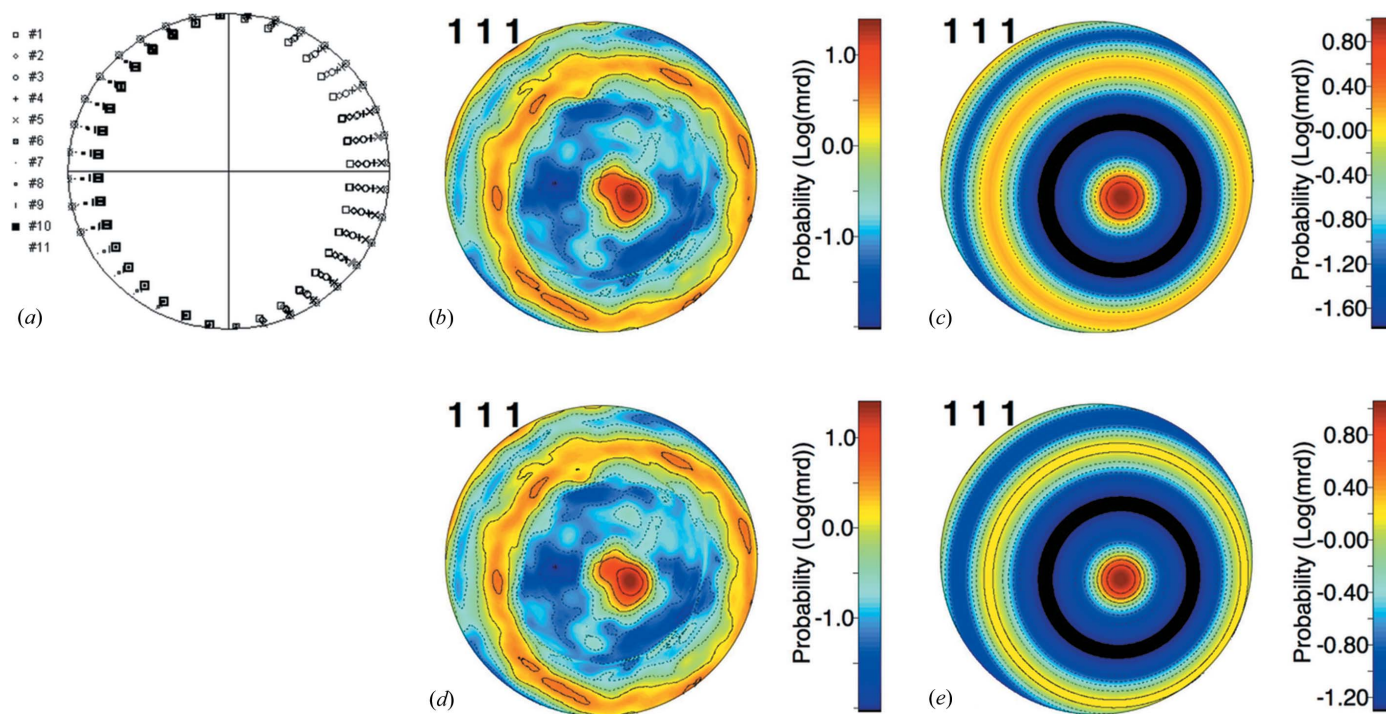
Figure 7
(*a*) Pole-figure coverage for all measured χ orientations, (*b*) {111}-recalculated pole figures using E-WIMV ODF refinement and Pawley structure-factor extraction method, (*c*) one fibre texture component and Pawley, (*d*) E-WIMV and kinematical plus Blackman structure-factor calculation and (*e*) fibre component and kinematical plus Blackman.

pole-figure coverage increases and all the ODF cells are defined by a minimum of 97 hints, corresponding to 100% ODF coverage (Fig. 7) and large redundancy. As usual in QTA obtained by transmission measurements, the relatively poorly covered pole figures can nevertheless result in a full coverage of the ODF because of an additional symmetry relationship induced by the crystal space group and by the large Q reachable over the small angular range. In this case we did not impose any sample texture symmetry using the E-WIMV (Lutterotti *et al.*, 2004) ODF refinement. In more delicate cases, additionally imposed texture symmetry could be used as the next constraint to compensate for the eventual missing ODF coverage. For instance, in the case of our Pt film we expect a cyclic fibre texture (Chateigner, 2010), *i.e.* with an axial, C_∞, symmetry axis perpendicular to the sample plane in which intensities are azimuthally independent. However, even in such simple samples and phases, most of the time the fibre axis is not strictly perpendicular (the cyclic character of the fibre is lost), and inclined fibre textures are found (Chateigner *et al.*, 1998). Both kinds of texture types can be imposed using standard function models (Lutterotti *et al.*, 2007; Matthies *et al.*, 1987), the spread (FWHM) and maximum orientation of which are refinable in a fit procedure thus applicable also when the ODF is not fully covered and discrete methods like E-WIMV cannot be applied.

The EPD patterns (Fig. 6*a*) are integrated along the Debye rings for a given angular range $\Delta\eta$, resulting in $2\pi/\Delta\eta$ one-dimension 2θ patterns (Figs. 6*b* and 6*c*), if we exclude unusable patterns corresponding to the blind area of the beam stop. $\Delta\eta$ are usually chosen in order to be adapted to the texture

strength, smaller $\Delta\eta$ values being required for sharper textures, and resulting in a larger number of patterns out of one diffraction image. We chose here $\Delta\eta = 10°$, a rather large integration angle compared to the standard 5° grid used in texture analysis, in order to homogenize over a large enough number of crystallites and ameliorate statistics. This step should be carefully examined since larger $\Delta\eta$ values accommodate poorer crystallite statistics but might artificially smooth the texture, while smaller values are needed to correctly simulate sharper textures giving rise to abrupt intensity variations along the Debye rings. Since our diffraction patterns exhibit some graininess (Fig. 6*a*), $\Delta\eta = 10°$ appeared as a good compromise with satisfactory statistics in the one-dimensional diagrams (Fig. 6*b*). Our integration range operated on the 11 diffraction images at varying tilts then resulted in 385 diffraction diagrams (also contributing to the large redundancy in ODF coverage). Fig. 6(*c*) reveals the strong intensity variations (already visible in Fig. 6*a*) along the Debye rings due to texture. These variations are not the same for different tilt values (as illustrated for extreme and at 0° tilt sample orientations under the electron beam) and must correspond to a single ODF.

We consequently imposed a discretization of the ODF into 10° Euler-angle cells for the E-WIMV algorithm used inside the Rietveld fitting. Such a cell size results in 12 960 ODF densities to refine for a triclinic space group, which reduces in our case to 150 because of cubic crystal symmetry, a rather small value compared to the number of data points in the pole-figure coverage. For diffracted intensity and structure-factor calculations during the Rietveld fits we have tested on one

hand Pawley and Le Bail pattern matching, and on the other hand kinematical calculation with the Blackman approach for partial dynamical corrections. Some discrepancies are observed between experimental and refined one-dimensional diagrams, which depend on the tilt angle and the model used to calculate structure factors (Fig. 6b). The two-dimensional plots (Fig. 6c) contain visually more information as the texture variations are expressed as vertical intensity variations for all the $\Delta\eta$ values for a given tilt. Comparing experimental (Fig. 6c, bottom two-dimensional plots) and ODF-recalculated (Fig. 6c, top two-dimensional plots) data at different tilt angles, one can see that experimental data are correctly reproduced. Specifically, intensity variations are simulated correctly for all sample tilts and all diffracted lines, i.e. a consistent ODF is able to represent the variations. The weighted reliability factors obtained for the global Rietveld fit (Rietveld, 1967) and for the ODF (Chateigner, 2005) are $R_w = 19.0\%$ and $R_w = 23.5\%$, respectively, for the Pawley extraction, attesting to a fairly good agreement. Such reliability factors might appear large but one has to bear in mind that R_w factors depend on the number of fitted points, which is here large compared to single diagrams in classical Rietveld analysis.

Fig. 7 reports the {111} pole figures recalculated from the refined ODF, for four different analyses using various models: the first two analyses used Pawley fitting with either E-WIMV ODF refinement (Fig. 7b) or a refined fibre standard function component (Fig. 7c), while the two others used the kinematical scattering structure-factor and intensity models corrected by the two-wave Blackman dynamic approach and either E-WIMV or standard fibre (Fig. 7d and 7e, respectively).

Using E-WIMV more local ODF variations can be revealed, up to (in this case) the statistical variation due to the reduced number of individual crystallites investigated by the small TEM spot (as in Fig. 5). Such local determination, repeated at several places in the sample, can be used to identify individual texture components later used in the refinement of the macroscopic ODF representing the sample using the standard function model. We used it here to filter out the 'noise' due to the reduced grain statistic. In this case the fibre standard component allowed us to refine exactly the inclination axis of the fibre component (16.7°) and its spread (14.0°) as illustrated in Figs. 7(c) and 7(e). For all practical purposes such a fibre model can then be used to predict macroscopic physical properties, e.g. sample elastic tensors, with much less calculation effort than using the full discretized ODF by E-WIMV.

The use of Blackman dynamical correction for structure factors shows a good agreement in texture results compared to Pawley extraction and Le Bail decomposition with $R_w(\text{Rietveld}) = 23.0\%$ and $R_w(\text{ODF}) = 24.1\%$. The maxima of density distributions on the {111} pole figure exhibit less than 0.5 m.r.d. (where m.r.d. = multiple of random distribution) difference compared to simple Pawley extraction. We conclude that on nanopowders the calculation of structure factors corrected for dynamical effect by this simple approach is sufficient to obtain a correct texture analysis. This is verified both within the use of either E-WIMV or standard functions.

6. Conclusion

This work demonstrates the quantitative use of EPD patterns to characterize almost routinely nanoparticles in the form of powders and thin films. The use of the combined analysis approach allows the quantitative determination of crystallite sizes and shapes, crystallographic texture and structural refinements. Working directly on two-dimensional EPDs offers the possibility of correcting for detector misalignments, positioning and slight changes from pattern to pattern. The incorporation of the two-wave dynamical correction for scattered intensity allows better refinements. Local variations of the texture are made feasible using this new development. The simple dynamical correction using Blackman theory is sufficient to correct the structural intensities in order to perform a quantitative texture analysis without resorting to a Le Bail fitting as done in Gemmi et al. (2011). In the future complementary measurements will be added, for instance energy-dispersive X-ray spectroscopy in order to constrain the refinements in cases for which elemental variations are important, and PDF, in order to quantify even amorphous structures (Cockayne & McKenzie, 1988; Petkov et al., 1998; Takagi et al., 2001).

This reciprocal-space approach allows fast access to statistically meaningful information about the average size and shape of an assembly of nanoparticles (agglomerated or not). It is thus very complementary to direct imaging of isolated nanoparticles and can be obtained on any transmission electron microscope. Fast and insensitive to sample drift, this approach may be advantageously used for gaining quantitative information from in situ environmental studies of dynamic processes involving nanoparticles [chemical reactions, redox chemistry, Ostwald ripening, phase transition (Luo et al., 2011) etc.].

References

Abeykoon, A. M. M., Malliakas, C. D., Juhás, P., Božin, E. S., Kanatzidis, M. G. & Billinge, S. J. L. (2012). Z. Kristallogr. 227, 248–256.
Alloyeau, D., Ricolleau, C., Oikawa, T., Langlois, C., Le Bouar, Y. & Loiseau, A. (2008). Ultramicroscopy, 108, 656–662.
Blackman, M. (1939). Proc. R. Soc. London Ser. A, 173, 68–82.
Carr, M. J., Chambers, W. F. & Melgaard, D. (1986). Powder Diffr. 1, 226–234.
Chateigner, D. (2005). J. Appl. Cryst. 38, 603–611.
Chateigner, D. (2010). Combined Analysis. London: ISTE–Wiley.

research papers

Chateigner, D., Wenk, H.-R., Patel, A., Todd, M. & Barber, D. J. (1998). *Integr. Ferroelectr.* **19**, 121–140.

Cockayne, D. J. H. & McKenzie, D. R. (1988). *Acta Cryst.* A**44**, 870–878.

Cowley, J. M. (2004). *Micron*, **35**, 345–360.

Database of Zeolite Structures (2014). http://www.iza-structure.org/databases/.

Denley, D. R. & Hart, H. V. (2002). *J. Appl. Cryst.* **35**, 546–551.

Downs, R. T. & Hall-Wallace, M. (2003). *Am. Mineral.* **88**, 247–250.

Ganesh, K. J., Kawasaki, M., Zhou, J. P. & Ferreira, P. J. (2010). *Microsc. Microanal.* **16**, 614–621.

Gemmi, M., Voltolini, M., Ferretti, A. M. & Ponti, A. (2011). *J. Appl. Cryst.* **44**, 454–461.

Gražulis, S., Chateigner, D., Downs, R. T., Yokochi, A. T., Quirós, M., Lutterotti, L., Manakova, E., Butkus, J., Moeck, P. & Le Bail, A. (2009). *J. Appl. Cryst.* **42**, 726–729.

Hammersley, A. P. (1998). *FIT2D Internal Report ESRF-98-HA01T*. ESRF, Grenoble, France.

Ischia, G., Wenk, H.-R., Lutterotti, L. & Berberich, F. (2005). *J. Appl. Cryst.* **38**, 377–380.

Kim, J.-G., Seo, J.-W., Cheon, J. & Kim, Y.-J. (2009). *Bull. Korean Chem. Soc.* **30**, 183.

Labar, J. L. (2009). *Microsc. Microanal.* **15**, 20–29.

Li, X. L. (2010). *Ultramicroscopy*, **110**, 297–304.

Luo, Z., Vasquez, Y., Bondi, J. F. & Schaak, R. E. (2011). *Ultramicroscopy*, **111**, 1295–1304.

Lutterotti, L. (2010). *Nuclear Instrum. Methods Phys. Res. Sect. B*, **268**, 334–340.

Lutterotti, L., Bortolotti, M., Ischia, G., Lonardelli, I. & Wenk, H.-R. (2007). *Z. Kristallogr. Suppl.* **26**, 125–130.

Lutterotti, L., Chateigner, D., Ferrari, S. & Ricote, J. (2004). *Thin Solid Films*, **450**, 34–41.

Lutterotti, L., Matthies, S., Wenk, H.-R., Schultz, A. J. & Richardson, J. W. (1997). *J. Appl. Phys.* **81**, 594–600.

Lutterotti, L., Pilliere, H., Fontugne, C., Boullay, P. & Chateigner, D. (2013). http://nanoair.dii.unitn.it:8080/sfpm and http://cod.iutcaen.unicaen.fr.

Lutterotti, L., Pilliere, H., Fontugne, C., Boullay, P. & Chateigner, D. (2014). *J. Appl. Cryst.* Submitted.

Lutterotti, L., Vasin, R. & Wenk, H.-R. (2014). *Powder Diffr.* **29**, 76–84.

Matthies, S., Vinel, G. W. & Helming, K. (1987). *Standard Distributions in Texture Analysis*, Vol. 1. Berlin: Akademie-Verlag.

Morales, M., Chateigner, D., Lutterotti, L. & Ricote, J. (2002). *Mater. Sci. Forum*, **408**, 113–118.

Palatinus, L., Jacob, D., Cuvillier, P., Klementová, M., Sinkler, W. & Marks, L. D. (2013). *Acta Cryst.* A**69**, 171–188.

Peng, L.-M., Ren, G., Dudarev, S. L. & Whelan, M. J. (1996). *Acta Cryst.* A**52**, 257–276.

Petkov, V., Holzhüter, G., Tröge, U., Gerber, Th. & Himmel, B. (1998). *J. Non-Cryst. Solids*, **231**, 17–30.

Popa, N. C. (1998). *J. Appl. Cryst.* **31**, 176–180.

Proffen, T. & Billinge, S. J. L. (1999). *J. Appl. Cryst.* **32**, 572–575.

Rauch, E. F. & Véron, M. (2005). *Mat.wiss. Werkst.tech.* **36**, 552–556.

Reddy, M. A., Kishore, M. S., Pralong, V., Caignaert, V., Varadaraju, U. V. & Raveau, B. (2006). *Electrochem. Commun.* **8**, 1299–1303.

Rietveld, H. M. (1967). *Acta Cryst.* **22**, 151–152.

Sicard, L., Le Meins, J. M., Méthivier, C., Herbst, F. & Ammar, S. J. (2010). *J. Magn. Magn. Mater.* **322**, 2634–2640.

Sinkler, W., Own, C. S. & Marks, L. D. (2007). *Ultramicroscopy*, **107**, 543–550.

Song, K., Kim, Y.-J., Kim, Y.-I. & Kim, J.-G. (2012). *J. Electron Microsc.* **61**, 9–15.

Spence, J. C. H. & Zuo, J. M. (1992). *Electron Microdiffraction*. New York: Plenum Press.

Takagi, T., Ohkubo, T., Hirotsu, Y., Murty, B. S., Hono, K. & Shindo, D. (2001). *Appl. Phys. Lett.* **79**, 485–487.

Tonejc, A. M., Djerdj, I. & Tonejc, A. (2002). *Mater. Sci. Eng. C*, **19**, 85–89.

Vainshtein, B. K. (1964). *Structure Analysis by Electron Diffraction*. London: Pergamon Press.

Weiland, H. & Panchanadeeswaran, S. (1993). *Textures Microtextures*, **20**, 67–86.

Weirich, T. E., Labar, J. L. & Zuo, X. D. (2006). Editors. *Electron Crystallography: Novel Approaches for Structure Determination of Nanosized Materials*, pp. 185–195. Dordrecht: Springer.

Weirich, T. E., Winterer, M., Seifried, S., Hahn, H. & Fuess, H. (2000). *Ultramicroscopy*, **81**, 263–270.

Weirich, T. E., Winterer, M., Seifried, S. & Mayer, J. (2002). *Acta Cryst.* A**58**, 308–315.

Williams, D. B. & Carter, C. B. (1996). *Transmission Electron Microscopy Part 1: Basics*. New York: Plenum Press.